Regulation Mechanism on a Bilayer Li_2O-Rich Interface between Lithium Metal and Garnet-Type Solid Electrolytes

Haoyang Jiang, Junqing Liu, Bin Tang, Zhendong Yang, Xinghui Liang, Xinyu Yu, Yirong Gao, Jinping Wei, and Zhen Zhou**

H. Jiang, Dr. J. Liu, Z. Yang, X. Liang, Prof. J. Wei, Prof. Z. Zhou

Institute of New Energy Material Chemistry, Key Laboratory of Advanced Energy Materials Chemistry (Ministry of Education), Renewable Energy Conversion and Storage Center (ReCast)

School of Materials Science and Engineering

Nankai University

Tianjin 300350, P. R. China.

Email: zhouzhen@nankai.edu.cn

Dr. B. Tang, Prof. Z. Zhou

Interdisciplinary Research Center for Sustainable Energy Science and Engineering ($IRC4SE^2$)
School of Chemical Engineering

Zhengzhou University

Zhengzhou 450001, P. R. China.

E-mail: tangbin@zzu.edu.cn

X. Yu, Y. Gao

University of Michigan-Shanghai Jiao Tong University Joint Institute

Shanghai Jiao Tong University, 800 Dong Chuan Rd., Minhang District

Shanghai, 200240, P. R. China

Author Manuscript

This is the author manuscript accepted for publication and has undergone full peer review but has not been through the copyediting, typesetting, pagination and proofreading process, which may lead to differences between this version and the Version of Record. Please cite this article as doi: 10.1002/adfm.202306399.

This article is protected by copyright. All rights reserved.

Keywords: Li_2O-rich interface, dynamic void evolution, interfacial Li^+ transportation, solid electrolytes, lithium metal batteries

Abstract: The practical implementation of garnet-type solid electrolytes, such as $Li_{6.4}La_3Zr_{1.4}Ta_{0.6}O_{12}$ (LLZTO), faces a significant challenge due to the presence of Li dendrites. Though artificial interfacial strategies have shown effective suppression of dendritic growth, further investigation is needed to understand the mechanism of achieving homogeneous Li deposition and its suitability for stable operation under real-world conditions. In this work, we construct a bilayer interface to address these issues. Such a bilayer interface consists of one conformal Li_2O-rich layer, generated by rubbing LLZTO pellets inside molten Li with low-dose In_2O_3, and another Li_2O layer deposited through atomic layer deposition (ALD). We explore the regulatory effect of the initial Li_2O-rich layer on achieving uniform Li deposition, promoting the critical current density (CCD) of 2.4 mA cm^{-2}. However, simple interfacial strategy is insufficient to prevent anodic degradation for cycling at room temperature without stack pressure, leading to increased current leakage directly reducing Li^+ within electrolyte. After insulating it with second ALD-Li_2O layer presenting minimal hamper on ionic conduction, the Li/Li symmetric cells achieves long cycling life exceeding 1000 h at 0.5 mA cm^{-2} and maintains stable operation even at 2 mA cm^{-2}. This work provides valuable insights for interfacial strategies towards practical operation of solid-state lithium metal batteries.

1. Introduction

Confronted with fast-growing electric vehicles and energy storage markets, conventional lithium-ion batteries manifest unexpected deficiencies such as capacity anxiety and safety issues.[1] These problems have propelled the development of solid-state batteries, in which the solid electrolyte is non-flammable and satisfies the pursuit of higher energy density when combined with Li metal anodes and high-voltage cathodes.[2] Garnet-type ceramics $Li_{6.4}La_3Zr_{1.4}Ta_{0.6}O_{12}$ (LLZTO) with high ionic

This article is protected by copyright. All rights reserved.

Author Manuscript

conductivity (up to 10^{-4}–10^{-3} S cm^{-1}) and better compatibility with Li metal, are identified as promising candidates for practical application.[3] Most importantly, the robust mechanical strength endows garnets potential to prevent hard breakdown.[4] However, Li dendrite formation can still be observed within garnets during battery operation, resulting in low critical current density (CCD) and deficient power density.[5]

Extensive research on the nucleation sites and stress-driven evolution of Li dendrites has led to a better understanding of the irregular Li deposition within limited interfacial contact area between garnets and metallic Li anodes.[6] First, the poor wettability of metallic Li, even molten Li, on primitive LLZTO surface leaves voids and/or gaps, which is responsible for large interfacial area specific resistance (ASR) ranging from 10^2–10^3 Ω cm^2.[7] Second, during the Li plating process, uneven distributed electrical field at these poor contact areas, would affect the inhomogeneous kinetics of Li nucleation.[8] According to previous reports, amplified electric filed, generating at the edge of voids, referred to as “tip effect”, would amplify the depositing current and accumulate stress simultaneously.[9] Especially under high current density, the stress concentration within the constrained space (such as voids and cracks) can reach up to several gigapascals, and even impel Li dendrite intragranular intrusion into solid electrolytes.[5,10] Third, the already existing grain boundaries and newly caused cracks inside the solid electrolyte pellet provide much favourable pathways for dendrite propagation.[11]

Author Manuscript

This article is protected by copyright. All rights reserved.

Author Manuscript

The introduction of lithiophilic interphases (such as Al, Ge and ZnO) to promote molten Li wettability has become a common strategy that can significantly reduce ASR at interface.[12] However, these batteries are hard to prove stable cycling with higher current density (exceeding 0.5 mA cm^{-2}), because of the ignorance of dynamically forming voids during alternative stripping and plating processes. The interfacial contact loss will occur due to the inevitable injection of vacancies at the interface, when the Li^+ depletion from the interface is fairly higher than the replenishment by Li self-diffusion and creep.[9c,13] The dynamic void expanding process can be depicted as electrochemical Ostwald ripening.[7,14]

Applying external pressure or high temperature facilitates metallic creep and atom diffusion to maintain interfacial contact during cycling, but may be unfavourable for commercialization.[15] Direct modification of the garnet surface or Li anodes, while creating artificial interface, proves valid to balance Li^+ flux and accelerate interfacial Li transportation.[16] It assists in the Li uniform deposition and maintains intimate interfacial contact even under practical conditions.[17] However, whether the thinner interfacial structure can completely suppress the generation of dynamic void, needs further exploration, for the interfacial modification strategy may less affect the anode structure, where voids still forming. Thus, it is of vital importance to determine whether such an artificial interlayer can withstand newly emerging dendrite inducements, and comprehensively evaluate the upper limit on promoting electrochemical performance for further guiding interfacial modification with lower expense and remarkable improvement.

This article is protected by copyright. All rights reserved.

Author Manuscript

In this work, we propose a precise bilayer Li_2O-rich interface for better electrochemical performance at higher current density and moderate operation conditions. For intimate interfacial contact, the LLZTO pellet was rubbed in molten Li with low-dose In_2O_3 (noted as Li-In_2O_3/LLZTO), gathering a Li_2O-rich layer attached to LLZTO. For electronic insulation, a 20 nm Li_2O layer (noted as Li-In_2O_3/Li_2O@LLZTO) was implemented by atomic layer deposition (ALD). As a result, better cell performance can be reached for Li-In_2O_3/Li_2O@LLZTO with the bilayer interface, realizing a cycling life up to 1000 h at 0.5 mA cm^{-2}, a CCD of 2.4 mA cm^{-2}, and a stable cycling even at 2 mA cm^{-2} at 30 °C without stack pressure.

In the Discussion section, we delved into the synergistic effects of the bilayer interface in preventing dendrite formation during cycling. Leveraging the stability and multi-pathways it provides for Li transport, the Li_2O-rich layer effectively relocates dynamic voids away from the LLZTO surface and confines them within the anodic bulk. This architectural feature plays a pivotal role in maintaining a uniform electric field distribution and facilitating Li^+ exchange flux at the interface, rendering the batteries resistant to the detrimental impacts of interfacial voids. Building upon this foundation, we examined the primary challenges that batteries face in maintaining stable performance, particularly in practical scenarios. The lithium metal anode inevitably experiences pulverization stemming from dynamic voids, which results in significant gaps during Li stripping and induces additional voltage polarization at the interface. Though this phenomenon exerts less influence on interfacial Li exchange, the LLZTO's

This article is protected by copyright. All rights reserved.

limited electron transfer capabilities contribute to increased current leakage within the electrolyte, accompanied by higher voltage levels.[11] This, in turn, directly fosters the initiation of Li dendritic growth. To address these challenges, we introduced an additional dense Li_2O layer to insulate electron flow. This innovative approach led to prolonged cycling life and stable performance, even at current densities approaching the CCD. Surprisingly, the Li_2O layer exhibited less impact on ionic conductivity compared with the commonly used LiF layer, which has adverse effects on battery performance. This accounts for the remarkable improvement in electrochemical performance observed in our study. The synergistic bilayer interface strategy presented here, based on a comprehensive analysis of interfacial and anodic evolution, serves as a valuable guide for advancing and innovating practical solid-state batteries under moderate operating conditions.

2. Results

2.1. Construction of a bilayer Li_2O-rich interface

Garnet-type LLZTO was selected as the solid electrolyte in this work. Ta was chosen to stabilize the high-ionic-conductivity cubic phase and avoid extra side reactions with Li.[18] The ceramic pellet was densified through a conventional pressure-free sintering process, with excessive LiOH and Al_2O_3 added to improve the sintering quality assisted with liquid phases.[19] The X-ray diffraction (XRD) patterns in **Figure 1**a can be indexed to cubic garnet phase (PDF#80-0457). The narrow and sharp peaks indicate the superior

Author Manuscript

This article is protected by copyright. All rights reserved.

crystallization, which significantly promotes the ionic conductivity. Thus, a high ionic conductivity was measured to be 0.48 mS cm^{-1} at room temperature (Figure S1, Supporting Information).

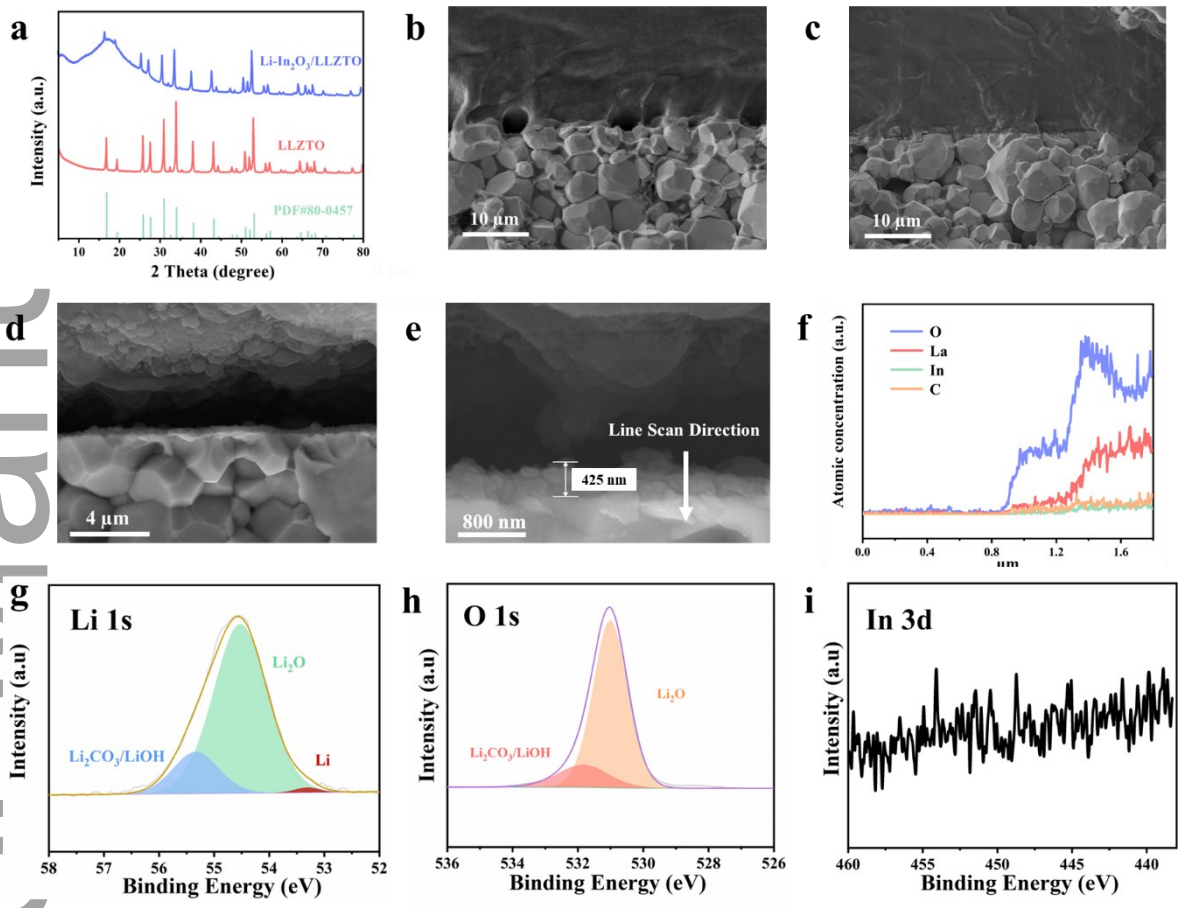


Figure 1. The morphology and constituent for the Li_2O-rich layer. (a) XRD patterns of a pure LLZTO pellet and a pellet with a Li_2O-rich layer exposed by long-time stripping of Li-In_2O_3/LLZTO. SEM images of the cross profiles for (b) pristine Li/LLZTO and (c) Li-In_2O_3/LLZTO. (d) SEM image of the interlayer between Li and LLZTO from cross-sectional view after 4 h stripping. (e) Amplified view of the exposed interlayer and (f) the corresponding line profile of O, La, C and In elements along the line scan direction shown in (e). (g-i) XPS analysis on the interlayer constituent by Li 1s, O 1s and In 3d spectra.

This article is protected by copyright. All rights reserved.

Author Manuscript

Author Manuscript

According to a previous report,[20] the surface of LLZTO presents intrinsic lithiophilic property. Nevertheless, LLZTO can react with the moist air to gather contaminations (such as Li_2O, LiOH, and Li_2CO_3) on the surface, which severely hamper the wettability of molten Li even with tiny residues.[21] Besides, the large surface tension of molten Li is another barrier to realize perfect wetting. As demonstrated in Figure S2 (Supporting Information), the molten Li is inclined in a spherical shape, and even after stirring and rubbing the pellet in it, Li still cannot completely cover the surface. To address the wettability issue, a small amount of In_2O_3 was added into molten Li (mass ratio of Li:In_2O_3=50:1), promoting the Li wettability by two aspects. For one thing, the as-produced Li_2O species and Li-In alloy through conversion and alloying reactions, respectively, can enhance the viscosity and reduce the surface tension of liquid Li, making molten Li easily cover the substrate in macroscope.[22] In addition, the as-product Li_2O species excluded from molten Li possess better affinity to surface contamination and assists molten Li in adhering to pellets.[23] As a result, rubbing pellets in it can realize perfect wettability (Figures S2d and S3, Supporting Information). Compared with pristine Li/LLZTO, the scanning electron microscope (SEM) images of cross-section view for the interface of Li-In_2O_3/LLZTO (Figure 1b and c) reveal more coherent and compact contact without apparent voids.

To visually investigate the microstructure of the interlayer, we fabricated symmetric cells with Li-In_2O_3/LLZTO and stripped it uniaxially at 0.2 mA cm^{-2} to separate the Li anode from LLZTO surface. The solid electrolytes and electrodes were assembled in

This article is protected by copyright. All rights reserved.

Author Manuscript

coin cells as depicted in the schematic illustration in Figure S4 (Supporting Information). Squashed nickel foam was used to eliminate the influence of external stacking pressure at the interface. Meanwhile, the operation temperature was kept at 30 °C, beneficial for the inspection of actual interfacial behaviour during cycling. After 4 h stripping, the bulk of Li metal anodes partially separated from solid electrolytes in some micro regions with the designed interlayer exposed, whose thickness was measured to be 425 nm (Figure 1d and e). This interlayer demonstrates a high uniformity on LLZTO surface without voids or cracks, which is consistent with the elemental line profile in Figure 1f. La is one of the characteristic elements of LLZTO, indicating the position of the solid electrolyte. The continuously distributed O from 0.8 to 1.2 μm without La indicates the close contact between interlayer and LLZTO, with the main component of the interlayer speculated to be Li_2O.

After completely stripping until reaching an open circuit, the Li metal anode can be readily detached from the pellet, offering a direct perspective to observe the interlayer. The top-view SEM images with different resolutions exhibit many clusters fixed on the surface (Figure S5, Supporting Information). The particle sizes around 200 nm with relatively uniform distribution can be in connection well with Figure 1e. As there is no Li plating process at this side, the abundant clusters cannot be metallic Li. Moreover, the corresponding energy dispersive spectroscopy (EDS) mapping also shows that O element is more concentrated on the clusters that can be inferred as Li_2O (Figure S6, Supporting Information). Most importantly, the defects on the LLZTO surface are fully

This article is protected by copyright. All rights reserved.

filled with clusters (Figure S5, Supporting Information), which shows potential suppression of the abnormal dendrite initiation at defects.

The XRD pattern (Figure 1a) of Li-In_2O_3/LLZTO after detaching the Li metal anode presents no distinct characteristic peak corresponding to Li_2O. It reveals that the Li_2O clusters may be poorly crystallized, or its content is below the detection limit. Then, the state of the interphase was detected by X-ray photoelectron spectroscopy (XPS), in which the binding energies of Li 1s at 54.5, 55.3 and 53.3 eV correspond well with Li_2O, Li_2CO_3/LiOH and metallic Li, respectively (Figure 1g).[22] The highest intensity of Li_2O peaks in Li 1s and also in O 1s spectra (Figure 1h) demonstrates that Li_2O is the main component of the interphase. Besides, the small amount of Li_2CO_3/LiOH should be attributed to the surface oxidation during the sample transfer. Even so, metallic Li could still be detected. In view of the compactness of the interphase and Li_2O tending to aggregate into clusters (Figure 1e), it can be reasonably speculated that the Li metal may fill the gaps among Li_2O clusters. In addition, an important phenomenon should be noted: the spatial distribution of In is inconspicuous as shown in Figure 1f and i. This may result from the insignificant amount of In_2O_3 added (2 wt% and 1.48 ‰ in volume) and all Li-In alloys dissolve completely in the bulk of Li anodes (Figure S3, Supporting Information).[24] Hence, the facilitation of Li conveyance by Li-In alloys in the interphase is weak.[16b,25]

Such a Li_2O-rich layer enables close contact between Li metal anodes and LLZTO, and is expected to redistribute the electric filed and regulate homogeneous Li deposition

This article is protected by copyright. All rights reserved.

Author Manuscript

at the interface.[26] Due to the nature of immovability and electrochemical inertness, Li_2O clusters will not participate in electrochemical reactions and can anchor the interlayers. Though the metallic Li in the interlayer may provide space to generate dynamic voids, the Li_2O clusters would restrain the enlargement of the voids and make them possible to be filled during subsequent plating. Notably, the consecutive metallic Li around Li_2O clusters exactly serves as pathways to replenish Li^+ consumption in electrolytes and move the as-deposited Li away, avoiding stress generation. Furthermore, the lithiophobic Li_2O species can reduce the deposition barrier due to its low lattice mismatch with Li, thereby facilitating planar Li diffusion along the surface and creating multiple pathways for Li transport.[25,27]

However, electrons can be injected into the LLZTO electrolyte easily through electronic conductor components inside the interlayer. Due to the reduced bandgap, the defects or grain boundaries of LLZTO pellets become potential channels for current leakage, promoting Li^+ reduction and nucleation directly inside the pellets.[28] Typically, electronically insulating layers are employed between Li metal anodes and solid electrolytes to inhibit current leakage. The LiF layer is often preferred due to its excellent insulating properties, making it a top choice for this purpose.[27,29] However, LiF layer is a poor Li^+ conductor and the resulting additional interfacial ASR will reduce the energy and power density of batteries. Nanoscale Li_2O thin film based on ALD technology draws our attention, because it not only is electrically insulating, but shows much faster Li^+ migration.[30] Besides, it might guide the formation of the Li_2O-rich

Author Manuscript

This article is protected by copyright. All rights reserved.

layer due to their intrinsic affinity, contributing to unrestricted Li^+ transport at the interface. More details will be discussed later.

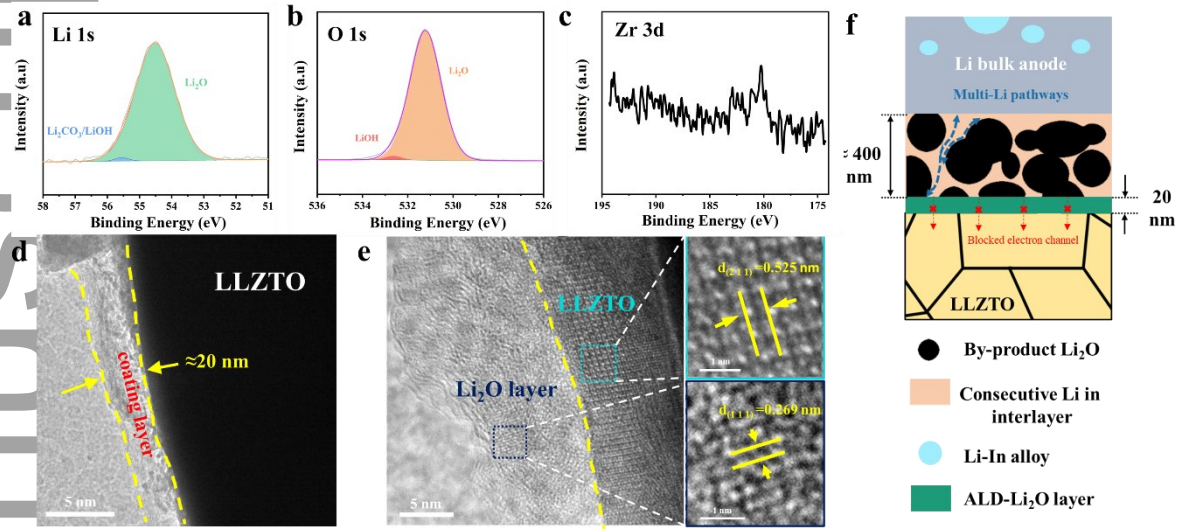


Figure 2. Characteristics of the ALD-Li_2O layer. (a-c) XPS analysis on ALD-Li_2O constituent by Li 1s, O 1s and Zr 3d spectra. (d) HRTEM images of the Li_2O coating on LLZTO surface and (e) corresponding interplanar spacing profiles of Li_2O and LLZTO species. (f) Schematic of the bilayer interface and corresponding Li transportation channels.

As presented in **Figure 2**a–c, the thin Li_2O layer prepared by ALD on LLZTO shows complete and homogeneous coverage, since the corresponding signal of Zr is absent and the main component was confirmed to be Li_2O. Then, we deposited a Li_2O layer with the same thickness on LLZTO powders, for the elaborate investigation by high-resolution transmission electron microscopy (HRTEM). The apparent lattice fringes with a *d*-spacing of 0.525 nm (Figure 2d-e) can be indexed into the (2 1 1) crystal plane of LLZTO, revealing that the as-prepared LLZTO particles are well crystallized.[31] The

This article is protected by copyright. All rights reserved.

Author Manuscript

compact Li_2O coating layer with a thickness of 20 nm was tightly attached to LLZTO, with the Li_2O species confirmed from enlarged regions by the *d*-spacing of 0.269 nm corresponding to the (1 1 1) crystal plane of Li_2O.[30b] Noteworthily, the ALD-Li_2O layer is polycrystalline and thin enough, where Li^+ migration with the aid of available vacancies or along crystal boundaries and amorphous regions may be reinforced.[30,32]

The schematic diagram of the interface is shown in Figure 2f, which contains two types of Li_2O, *i.e.*, the Li_2O-rich layer from In_2O_3 reacting with Li, and the ALD-Li_2O layer. Abundant and electrochemically inactive Li_2O clusters constitute the skeleton of the Li_2O-rich layer that reaches conformal coverage on LLZTO surface. Meanwhile, a small amount of permeable Li among the Li_2O clusters, act as bridges to maintain favourable Li transportation. Profiting from the fine structure, the deposited Li can be timely transported away from the LLZTO surface. This avoids the further deposited Li accumulating beneath the Li_2O-rich layer, which will destroy the interphase and generate stress to induce dendrites. Besides, the ALD-Li_2O layer serves as an insulating barrier to suppress detrimental current leakage into the solid electrolytes. Profited by its better ionic conductivity, the thicker ALD-Li_2O layer (20 nm) can be deposited to fully cover the defects on LLZTO without causing ASR increase.

2.2 Electrochemical performance of solid-state batteries

The electrochemical performances of LLZTO with different modified interfaces were preliminarily evaluated *via* electrochemical impedance spectroscopy (EIS) and CCD measurement in Li/Li symmetric cells. The Nyquist plots in **Figure 3**a show the ASR

This article is protected by copyright. All rights reserved.

Author Manuscript

Author Manuscript

subjected to the frequency range applied, with the two ends of semicircles representing the bulk and grain boundary resistance (high frequency), and interfacial resistance (medium frequency). After fitting with the equivalent circuit depicted in the inset of Figure 3a, the ASR for Li-In_2O_3/LLZTO interface is calculated to be 23 Ω cm^2. This indicates the optimized physical contact and unimpeded Li^+ transfer at interface with the aid of conformal Li_2O-rich layer. In comparison, the ASR of 52 Ω cm^2, is exhibited for the pristine Li/LLZTO interface, whose poor contact located at some micro regions or cracks as shown in Figure 1b would disturb interfacial electric field and expedite dendrite formation.[33] Meanwhile, the ASR is only 22 Ω cm^2 for Li-In_2O_3/Li_2O@LLZTO interface, supporting the negligible effects of ALD-Li_2O layer on hindering Li^+ transfer as discussed above.

This article is protected by copyright. All rights reserved.

Author Manuscript

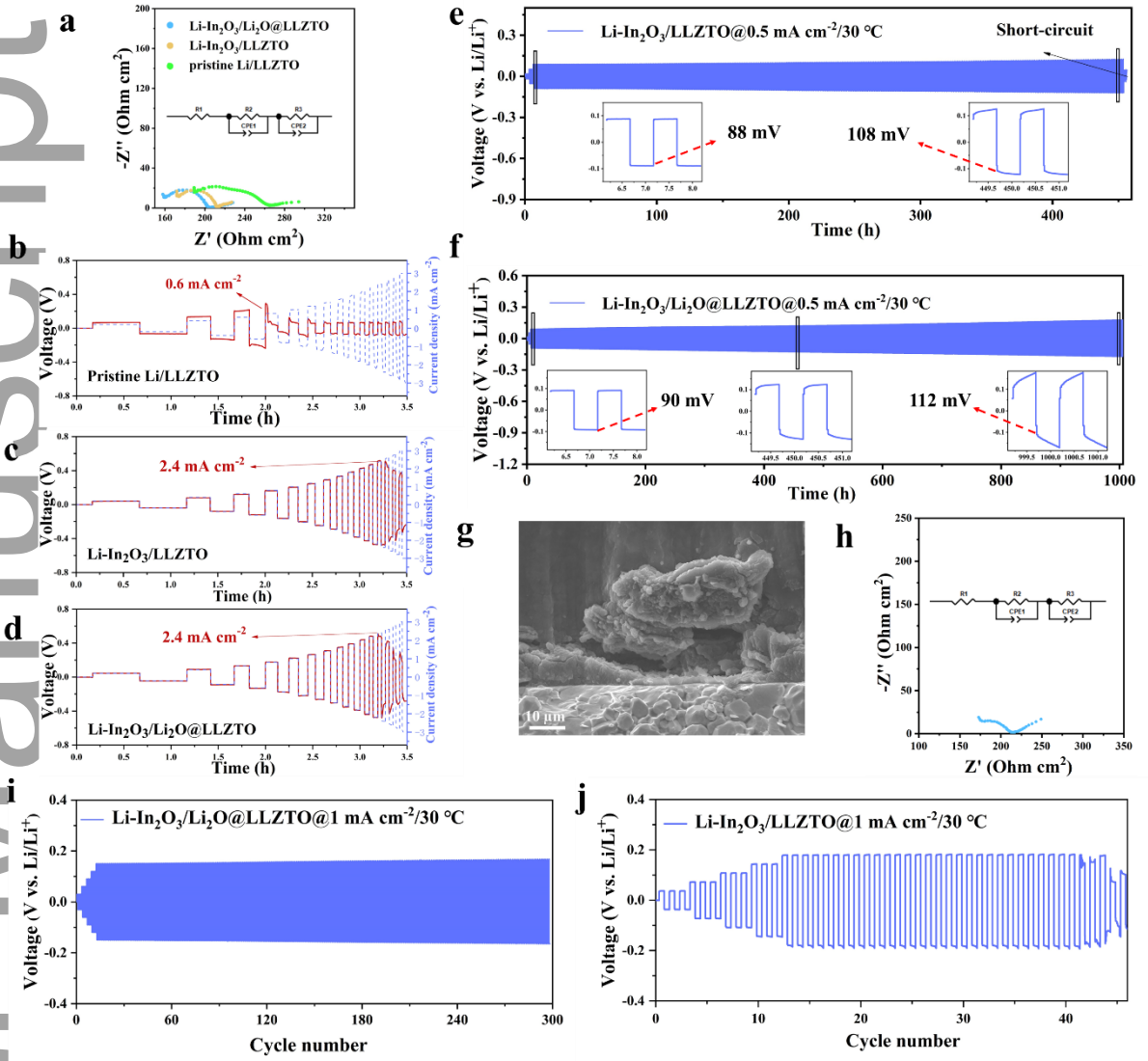


Figure 3. Electrochemical performance of Li/Li symmetric cells with different interlayers. (a) EIS measurement of Li/Li symmetric cells with or without interlayer at room temperature. The schematic of equivalent circuit is shown in the inset. (b-d) CCD measurement with stepwise increased current. Galvanostatic cycling performance for (e) Li-In_2O_3/LLZTO and (f) Li-In_2O_3/Li_2O@LLZTO at 0.5 mA cm^{-2}, with a corresponding capacity of 0.25 mAh cm^{-2}. (g) Cross-section image for Li-In_2O_3/LLZTO after cycling of 200 h at 0.5 mA cm^{-2}. (h) ASR measured for Li-In_2O_3/Li_2O@LLZTO after 700 h. Galvanostatic cycling performance for (i) Li-In_2O_3/Li_2O@LLZTO and (j) Li-In_2O_3/LLZTO under 1 mA cm^{-2}, with a capacity of 0.25 mAh cm^{-2}.

This article is protected by copyright. All rights reserved.

Author Manuscript

The CCD was tested by galvanostatic charge and discharge cycling under stepwise increased currents, until a sudden descend of voltage polarization (soft breakdown). As shown in Figure 3b-d, a notable CCD increase to 2.4 mA cm^{-2} is yielded for Li-In_2O_3/LLZTO and Li-In_2O_3/Li_2O@LLZTO, in stark contrast to the 0.6 mA cm^{-2} for pristine Li/LLZTO. The evident promotion certifies the effective restraint of Li dendrite initiation by homogenizing the electric field and Li^+ transportation at the interface, with Li_2O-rich layer. For further improvement of CCD performance, it is essential to consider the intrinsic nature of LLZTO ceramics (defect density, hardness, fracture toughness, *etc.*).[4] Further, the cycling performance was tested at 0.5 mA cm^{-2} with a capacity of 0.25 mAh cm^{-2}, where showing a strong performance contrast. As shown in Figure 3e, Li-In_2O_3/LLZTO presents a cycling life of 450 h before hard breakdown. Note that the flat voltage profiles at the beginning change into slow-growth profiles after 450 cycles, with the starting voltage polarization of stripping process increasing from 88 mV to 108 mV (zoom-in figures in Figure 3e). The elevated voltage polarization will contribute to the increase of current leakage and further dendrite generation inside the LLZTO pellets.[28c] Cross-section SEM images of Li-In_2O_3/LLZTO after 200 h cycling were utilized to interpret this phenomenon (Figure 3g and Figure S7, Supporting Information). Astonishingly, the bulk Li anode pulverizes and there is even a gap at interface, which would cause the shrunken contact area between anode and LLZTO during Li stripping, accounting for the slow-growth voltage profiles.[9c] This will be discussed in details later.

This article is protected by copyright. All rights reserved.

Author Manuscript

Profited from the restraint of current leakage by introducing ALD-Li_2O layer, the cycling time prolongs up to 1000 h for Li-In_2O_3/Li_2O@LLZTO. (Figure 3f) Intriguingly, the increase of ASR is much less after cycling for 700 h at 0.5 mA cm^{-2} (Figure 3h), emphasizing the validity of maintaining intimate interfacial contact by the Li_2O-rich layer. On the other side, it becomes evident that a straightforward enhancement of interfacial stability can indeed improve CCD measurements. However, it falls short in preserving the integrity of the anodic structure, posing a potential threat to overall cycling performance. The noteworthy disparity in cycling life between the two samples, despite both exhibiting the same CCD, provides compelling evidence for the efficacy of our synergistic interfacial strategy. Moreover, this contrast becomes even more striking when cells are subjected to testing under higher current densities, which can lead to increased voltage polarization in accordance with Ohm's law. For a current density of 1 mA cm^{-2}, a dendrite-free behaviour was found for Li-In_2O_3/Li_2O@LLZTO during 300 cycles as expected (Figure 3i), while Li-In_2O_3/LLZTO encountered breakdown after 30 cycles (Figure 3j). Astonishingly, Li-In_2O_3/Li_2O@LLZTO can operate at 2 mA cm^{-2} that approaches the CCD, despite the large voltage polarization of 350 mV (Figure S8, Supporting Information). Its high current tolerance validates the rationality of the synergistical bilayer strategy for achieving high power density in solid-state batteries at moderate circumstance.

This article is protected by copyright. All rights reserved.

Author Manuscript

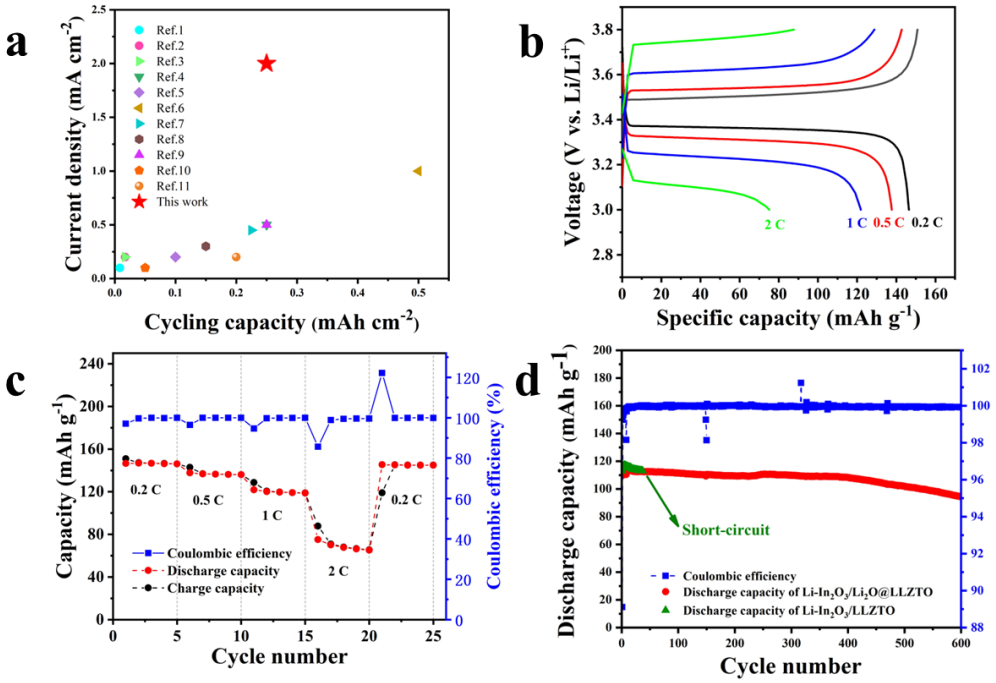


Figure 4. Performance comparison for symmetric cells with previously reported results and electrochemical tests in full cells at 30 °C. (a) The performance comparison of symmetric cells with garnet-type solid electrolytes and metallic Li anodes with previously reported results. The references are summarized in Table S1 (Supporting Information). (b) The discharge and charge curves for the full cells with Li-In_2O_3/Li_2O@LLZTO at different current rates from 0.2–2 C. (c, d) The rate performance and long-time cycling stability of the full cells with Li-In_2O_3/Li_2O@LLZTO.

Although, numerous interfacial strategies focus on the improvement of Li wettability, the suppression of dynamical voids or current leakage issue was ignored, presenting deficient high-rate performance and short durability (**Figure 4**a). Therefore, the stable operation at the current density (2 mA cm^{-2}) approaching the CCD value, here, conforms the triumph of the interfacial strategy. Further, the validity of this designed bilayer interface was verified in full cells, assembled with commercial $LiFePO_4$ (LFP, 170 mAh

This article is protected by copyright. All rights reserved.

g^{-1} in theoretical capacity), Li metal and Li-In_2O_3/Li_2O@LLZTO as the cathode, anode, and solid electrolyte, respectively. A slight amount of cathode wetting agent was added for better Li^+ transfer. As shown in Figure 4b, the full cells exhibit initial charge and discharge capacities of 150.9 and 146.5 mAh g^{-1} at 0.2 C, respectively, with the initial coulombic efficiency up to 95%. A small voltage hysteresis of only 0.13 V also indicates the negligible limit of Li^+ transfer kinetics often present at the anodic interface.

As shown in Figure 4c, the full cell exhibits reversible discharge capacity of 146.5, 137.7, 121.9 and 75.1 mAh g^{-1} at 0.2, 0.5, 1 and 2 C (2 C equals to 0.63 mA cm^{-2}), respectively. When the current returns to 0.2 C, the discharge capacity recovers to the initial value of 145.4 mAh g^{-1}. For the cycling stability, the full cell with double interlayer performs cycling life exceeding 600 cycles at 1 C with a capacity retention of 84% (94.4 mAh g^{-1}) at room temperature without external pressure. In comparison, the control sample with Li-In_2O_3/LLZTO quickly falls into short circuit after only 50 cycles (Figure 4d). This obvious contrast supports the validity that ALD-Li_2O layer can improve the operation stability by resisting current leakage. Moreover, we subjected the full cells to rigorous testing at an elevated current density of 2 C, as visualized in Figure S9 (Supporting Information). The noteworthy achievement of sustaining a prolonged cycling life of 400 cycles, coupled with minimal capacity decline, unequivocally signifies that the anode side, when endowed with a well-considered interfacial design, will not be an impediment to the advancement of solid-state battery technology.

Author Manuscript

This article is protected by copyright. All rights reserved.

Author Manuscript

3. Discussion

3.1. Dendrite suppression mechanism of the Li_2O-rich layer

According to above electrochemical results, constructing double-synergistic interlayer to maintain interfacial contact and against current leakage, can significantly promote cycling stability even at higher current density. In this section, we traced the Li deposition process with and without artificial interlayer to reveal the mechanism on dendrite suppression, and explored what is the biggest threat for prolonging cycling life at moderate operation circumstance. It can be expected as an important indicator to further optimize the interfacial strategy with better performance and lower cost. Here, Li_2O clusters do not participate in the chemical and electrochemical reactions meanwhile facilitate ion conduction, making it a suitable candidate for studying the dynamic stability of interface.

This article is protected by copyright. All rights reserved.

Author Manuscript

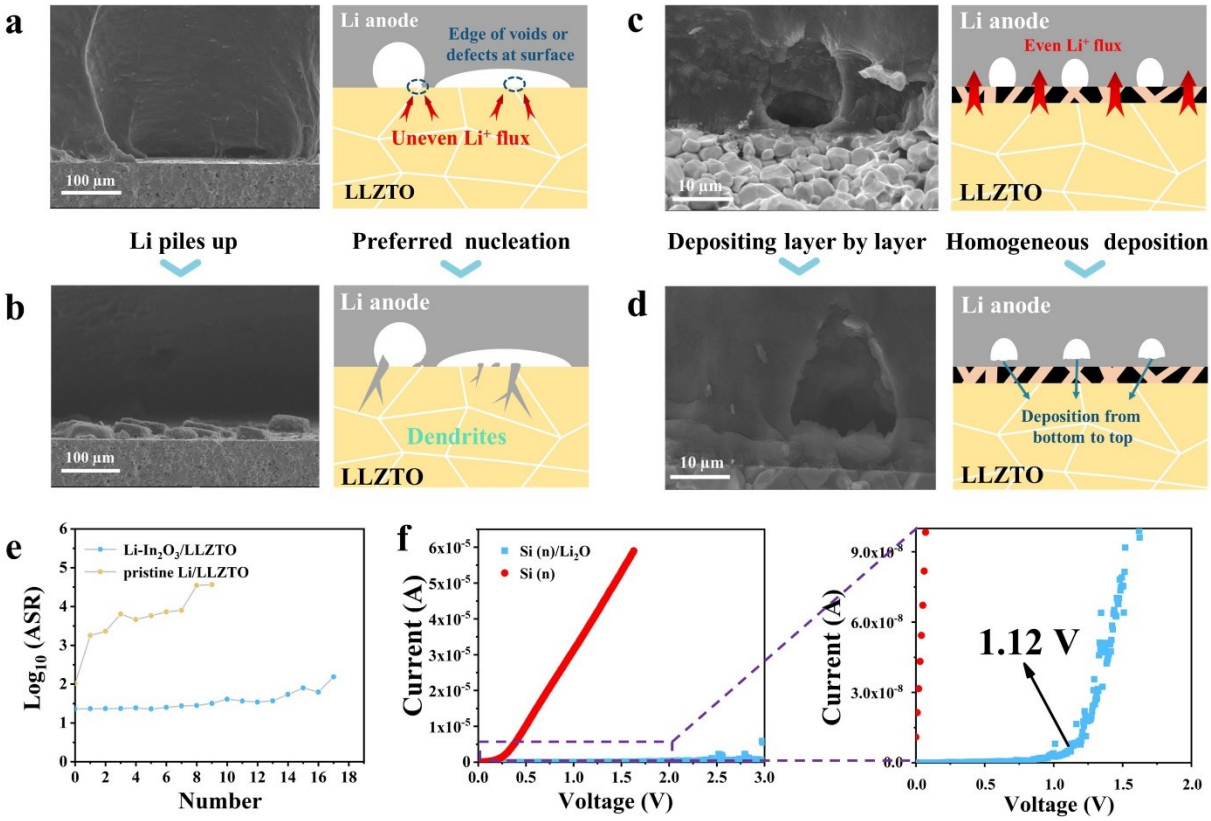


Figure 5. Mechanism of suppression preferred dendrites and current leakage. (a) Cross-section SEM image of the interfacial morphology of pristine Li/LLZTO after stripping for 0.4 mAh cm^{-2} and corresponding schematic. After plating for 0.2 mAh cm^{-2}, the irregular Li lumps grew on the LLZTO surface as depicted in (b) cross-section SEM image and schematic. Cross-section SEM images of the interfacial morphology and corresponding schematics of Li-In_2O_3/LLZTO after stripping for 0.4 mAh cm^{-2} (c) and then plating for 0.2 mAh cm^{-2} (d). (e) The ASR of interface evolution with relationship to the depth of stripping. The interval is 2 mAh cm^{-2}. (f) The detection of current leakage under ever-increased voltage.

SEM was used to monitor the morphologic evolution of the interface and deposited Li. The cells with pristine Li/LLZTO and Li-In_2O_3/LLZTO were stripped for 0.4 mAh cm^{-2} and then plated for 0.2 mAh cm^{-2} at 0.2 mA cm^{-2}. For pristine Li/LLZTO, due to

This article is protected by copyright. All rights reserved.

Author Manuscript

the poor wettability, there are many primary voids at the interface. Preferential Li stripping at the edge of gaps or voids will further enlarge their volume up to hundreds of micrometres with the pellet exposed (**Figure 5**a and Figure S10, Supporting Information).[9c] Thus, after plating reversely for 0.2 mAh cm^{-2}, the uneven Li deposition can be directly observed on bare LLZTO (Figure 5b and Figure S11, Supporting Information). Conforming to previous reports, Li primarily nucleates at surface defects or cracks, based on the surface chemical composition or mechanical character.[9a,34] Further, restricted to the slow surface diffusion kinetics of Li atoms, the deposited Li tends to grow vertically rather than laterally, especially when the plating current is relatively higher.[10b,35] As a result, it can be expected that Li nucleates and piles up at these favourable sites, meanwhile, with huge mechanical stress that generats from further local Li deposition beneath the lumpish Li, inducing dendrite to intrude the electrolyte. (Figure S11b, Supporting Information).

In stark comparison, for Li-In_2O_3/LLZTO after stripping for 0.4 mAh cm^{-2} (Figure 5c and Figure S12, Supporting Information), there are many voids with nearly the same size (around 10 μm in diameter) forming at the interface. Notably, the conformal Li_2O-rich layer is apparently attached with the pellet, with the voids located above the Li_2O-rich layer rather than adjacent to the LLZTO surface. This means a coherent interface between the Li_2O-rich layer and LLZTO surface. Profited by the regulated electric field at the void-free interface and evenly distributed multi-Li pathways inside Li_2O-rich layer, the exchanged Li^+ flux will be homogeneous. Subsequently, it contributes to the

This article is protected by copyright. All rights reserved.

layer-by-layer deposition and the avoidance of stress accumulation, both significantly suppressing dendrite initiation (Figure 5d and Figure S13, Supporting Information).

3.2. Increased voltage polarization from anodic pulverization

Now that the deposited Li can be regulated beyond the Li_2O-rich layer, why does a large portion of the Li metal anode turn into porosity (*i.e.*, theoretically only 1.25 μm lithium will participate in the electrochemical reaction in Figure 5e-h) after long-time cycling? It could lead to expedited shrink of the contact area during stripping and constriction resistance.[7,34] The resultant extra voltage polarization is indispensable to transport sufficient Li from the bulk to the interface, responsible for the slow-growth profile in Figure 3e.[36] As the Li metal anode above this porous area still keeps intact, the probability of corrosion by the air can be excluded (Figure S7, Supporting Information). Then, we reasonably speculate this phenomenon stemming from the irreversibility between Li stripping and plating process. Due to the slow Li transportation kinetics in the anode bulk, the dynamically forming voids are inevitable when operating at moderate circumstance. They trigger uneven areal distribution of the Li stripping flux inside the anode bulk. Meanwhile, thanks to the regulatory effect of Li_2O-rich layer, the Li plating process will be homogeneous, causing that the dynamically forming voids during stripping cannot be filled during the subsequent plating process. As shown in Figure S14 (Supporting Information), after a complete cycle at 0.4 mAh cm^{-2}, there are many partially filled voids at the interface, evidencing this inference. In addition, such phenomenon would be more prominent under higher current density, since the Li

This article is protected by copyright. All rights reserved.

Author Manuscript

deposition into compact morphology only occurs at lower current density.[37] At higher deposition rates, the deposited Li crystalizes into smaller grains, severely preventing Li fusing into compactness.[38]

Intriguingly, despite the anodic pulverization existing, the conformal Li_2O-rich layer and intimate contact with LLZTO change slightly after long-term cycling (Figure 3g and h), signifying the homogeneous and steady Li^+ transfer at the interface. The evolution of ASR during uniaxial stripping was checked by EIS. For pristine Li/LLZTO interface (Figure 5e), the ASR rises suddenly at the beginning from 51 to 894 Ω cm^2, in connection with the contact loss. In striking contrast, the ASR of Li-In_2O_3/LLZTO interface basically remains unchanged, while a sharp increase happens near the point that the cell turns into open-circuit state. The less variation of ASR reveals that the void generation or even Li metal anode separation presents no influence for Li_2O-rich layer on the intimate attachment with the pellet. It can also manifest that the increased current leakage after long-term cycling is the dominant factor for dendrite generation. Further, we demonstrate the same tendency of ASR variation at 0.8 mA cm^{-2}, drawing the same conclusion that the robust Li_2O-rich layer cannot be ruptured by the quick generation of dynamic voids (Figure S15, Supporting Information).

According to the incoherent model proposed by Yang *et al.*,[13] the low Li self-diffusion (5.6×10^{-11} cm^2 s^{-1}) by defects in the metal bulk is far below the consumption in solid electrolytes (2.15×10^{-9} cm^2 s^{-1}).[9b] Running cells at high temperature (up to 100 °C) or exerting external pressure (around 50 MPa) can promote self-diffusion and

This article is protected by copyright. All rights reserved.

Author Manuscript

Author Manuscript

metallic Li creep to accelerate Li transportation, while avoiding the generation of dynamic voids.[13,15a] In this work, a Li_2O-rich layer constructed on the solid electrolyte conformally, can also bring positive impact on stable cycling particularly at practical conditions. This approach indirectly mitigates the adverse effects of dynamic voids, which can disrupt Li deposition and accumulate stress, potentially leading to dendrite formation at the interface. The formation of dynamic voids is isolated from the LLZTO surface and contained within the Li metal, effectively segregating them. This process results in the creation of a Li_2O-rich layer that plays a crucial role in balancing Li^+ ion exchange at the interface and facilitating the transport of deposited Li.

However, it is important to note that the moderate operating conditions, specifically at 30 °C without external stacking pressure, may not provide sufficient control over compact Li deposition. Consequently, the further deterioration of anodes can be attributed to the additional voltage polarization at the interface. This polarization has the potential to induce current leakage within the electrolyte, directly triggering dendrite formation. Similarly, when operating at higher current densities, the elevated voltage polarization, in accordance with Ohm's law, exacerbates current leakage. This poses a significant risk to the electrolyte, potentially leading to degradation or dendritic attacks.In this work, we introduced another layer of Li_2O insulation, which can be readily deposited with ALD technology. This layer offers notable advantages, including uniform coverage, even in the presence of defects, and high ionic conductivity. As a result, it can effectively double the cycling life, extending it up to 1000 h at a current

This article is protected by copyright. All rights reserved.

density of 0.5 mA cm^{-2}, and it maintains stable cell performance even at current densities approaching the CCD.

3.3. Superiority of the ALD-Li_2O layer

In this section, the protective effect of the ALD-Li_2O insulating layer against current leakage was checked firstly, to demonstrate its superiority. Due to the rather higher ionic conductivity of LLZTO, the detection of current leakage will be covered by ionic current. Thus, we chose the silicon wafer (*i.e.*, an n-type semiconductor) covered by the ALD-Li_2O layer to evaluate the ability of preventing current leakage. During measurement, a continuously increasing voltage was inflicted on the Au electrodes at both sides. The heteroatom doping inside silicon wafer can strengthen the electronic transportation, and induces current leakage increment along with ever-increased voltage polarization (Figure 5f). In contrast, the current maintains relatively stable below several nanoamps for the ALD-Li_2O coated wafer until the voltage polarization increases to 1.12 V, signifying the excellent inhibition of leakage current. Despite the sharp piercement by electrons afterwards, the protective effect of the ALD-Li_2O layer is remarkable, for the electronic conductivity of LLZTO is relatively weak.

Further, the advantage of high Li^+ conductivity is evaluated by comparing with the LiF layer. The LiF layers with better crystallinity constructed by ALD were controlled with the thickness of 2, 5 and 10 nm, and then the pellets were wetted with molten Li added In_2O_3. All the pellets exhibited great wettability. The influence on ionic conductivity was evaluated by EIS. As exhibited in Figure S16 (Supporting

This article is protected by copyright. All rights reserved.

Author Manuscript

Author Manuscript

Information), the interfacial ASR for cell with 2 nm LiF layer is 23 Ω cm^2, which resembles the result in Li-In_2O_3/LLZTO. However, when the thickness increases to 5 and even 10 nm, the interfacial ASR sharply increases to 46 and 60 Ω cm^2, respectively. The monotonic variation emphasizes the low ionic transportation kinetics in the LiF layer, restricted to which, the CCD declines to 1 mA cm^{-2} for the cell with a 2 nm LiF layer and further 0.8 mA cm^{-2} for 5 nm (Figure S17, Supporting Information). This hinderance for ionic transfer particularly gathering Li^+ at the solid electrolyte side will cause huge voltage polarization and further severe current leakage across the unavoidable defects inside the LiF layer. By contrast, the higher ionic conductivity of ALD-Li_2O layer makes it probably thicker and with less defects, beneficial for perfectly covering the surface of LLZTO. Thus, it demonstrates the importance of assessing the hindrance on ionic conduction when constructing artificial interlayers.

4. Conclusion

The aim of this study is to investigate the process of Li deposition in garnet-based solid-state lithium batteries and evaluated the validity of interfacial strategy, accompanying with the interface morphology evolution, when operating at moderate temperature without extra pressure. By reasonably combining byproduct-Li_2O from chemical reactions and ALD-Li_2O species in the interlayer, the negative influence of dynamically forming voids and inevitable current leakage is eliminated simultaneously. The generation sites of dynamic voids and even further pulverization of anodes are shifted away from the garnet surface, maintaining smooth Li^+ transfer at interface. Besides, the

This article is protected by copyright. All rights reserved.

Author Manuscript

tolerance of increased voltage polarization can be improved by the insulating ALD-Li_2O layer. Therefore, the growth of Li dendrites is controllable during prolonged cycling even under high current density. The symmetric cell displays a prolonged cycling life under moderate conditions without stacking pressure. Meanwhile, high-rate capacity can be reached in full cells paired with $LiFePO_4$ cathodes, which reveals an enhanced resistivity to Li dendrites and the improved security attributes. We believe that this comprehensive protocol on interfacial modification provides a feasible assessment for practical application that needs relatively moderate working conditions.

5. Experimental Section

Preparation of LLZTO electrolytes: The garnet-type $Li_{6.4}La_3Zr_{1.4}Ta_{0.6}O_{12}$ electrolyte was prepared *via* a conventional solid-state sintering method. $LiOH·H_2O$ (Aladdin, ≥99%), La_2O_3 (Aladdin, ≥99%, heated at 900 °C for 8h to remove H_2O), ZrO_2 (Macklin, >99.99%), and Ta_2O_5 (3A, >99.9%) were used as precursors. $LiOH·H_2O$ with 10 wt% excess was utilized to compensate the Li loss during sintering at high temperature and 2 wt% Al_2O_3 (Macklin, >99.99%) was added intentionally as a sintering aider. Stoichiometric amounts of starting materials were firstly ball milled in 2-propanol, after evaporating the solvent, and then calcined at 900 °C for 12 h at a corundum crucible. The calcinated powder was pulverized *via* high-speed ball-milling and subsequently pressed into pellets with a diameter of 12 mm. The as-pressed pellets were muti-step sintered, in which the first step was sintered at 1100 °C for 4 h, and then the temperature increased to 1150 °C for the other 4 h. The as-prepared pellets with a thickness around 700 μm and mass of 0.43 g, were polished with 600, 2000, 3000, and 5000

This article is protected by copyright. All rights reserved.

grit sandpapers to obtain a smooth surface. To avoid the facile corrosion by moisture, the pellets were stored in an Ar-filled glovebox with the concentration of O_2 and H_2O < 0.1 ppm.

Interface modification: Li tablets were melted in a stainless-steel container at 240 °C on a hot plate. The surficial oxidation layer was elaborately removed by tweezers until the molten Li shaped in spherical with metallic luster. In_2O_3 (MREDA, >99.995%) was added (with the mass ratio of 1:50 of In_2O_3:Li) into the container with subsequent stirring for around 10 s. Then, we dipped the pellets in molten Li several times till the composites covered the surface well. By rubbing the pellets against the bottom of container, the Li_2O product can be consolidated evenly on the surface and even in defects. Note that all the synthesis processes were completed in the glovebox. Compact Li_2O and LiF thin films were deposited on the surface of LLZTO by ALD process, performed in a custom reactor (MNT-S ALD, MNT Micro and Nanotech Co., Ltd). The ALD system was sustained at 0.4 torr by using a vacuum pump. Nitrogen (99.999%) was used as the carrier and purge gas with a flow rate of 20 sccm. Lithium tert-butoxide (LiO*t*Bu, 97%, Sigma-Aldrich) as the Li precursor was kept at 165 °C in stainless steel bottles with bubblers. For Li_2O layer, deionized water as oxygen precursor was kept at 25 °C The deposition temperature was 250 °C, and ALD pipelines were held at 200 °C to avoid precursor condensation. The pulse/purge time used in one ALD cycle was 1 s/10 s for LiO*t*Bu and 20 ms/10 s for H_2O. The deposition rate was close to 0.01 nm/cycle. For LiF layer, the fluorine precursor is Titanium Tetrafluoride, with the deposition temperature of 250 °C. The pulse/purge time used in one ALD cycle was 1 s/10 s for LiO*t*Bu and 200 ms/10 s for TiF_4.

This article is protected by copyright. All rights reserved.

Author Manuscript

Materials characterizations: The crystal structure was characterized by XRD (Rigaku Ultima IV), by using Cu-Kα radiation in the 2θ range of 5–80° with the rate of 10° min^{-1}. The elemental distribution and morphology of the interlayer were explored with EDS and field emission SEM (FE-SEM, JSM-7800F), respectively. The chemical constituents of the interlayer were identified *via* XPS (Thermo Scientific ESCALAB 250Xi). During sample transfer, a sealed cabin was utilized to avoid direct contact with moist air. The morphology and crystal structure of ALD-Li_2O coating layer was observed *via* HRTEM (JEM-2800). As for sample preparation, the LLZTO powders were dispersed on a silicon wafer, as the substrate to load LLZTO powders deposited with Li_2O *via* ALD. After sonicating the coated LLZTO powders in absolute ethyl alcohol, the copper wire mesh loaded samples was dried under laboratory conditions, and then, transferred for measurement rapidly.

Electrochemical measurements: The ionic and current leakage were measured with Au electrode. The ionic conductivity of LLZTO and interfacial specific aera resistance were calculated from EIS (Zahner) with the frequency from 1 MHz to 0.05 Hz at room temperature. Li-Li symmetric cells with different modified interfaces were assembled in 2032-type coin cells with nickel foam to avoid extra pressure. The stripping process under constant current was managed by LAND battery testers. The CCD value was measured by galvanostatic cycling from 0.2 mA cm^{-2} with a current increasement of 0.2 mA cm^{-2} at 30 °C. The cycling performances at current density of 0.5, 1, and 2 mA cm^{-2} were fixed in a certain capacity of 0.25 mAh cm^{-2} to avoid the adverse effect from deterioration of bulk Li, with the operation temperature of 30 °C.

Author Manuscript

This article is protected by copyright. All rights reserved.

Full cell assembly: $LiFePO_4$ was chosen for the stable voltage plateau. To assemble the full cells, LFP powder, Ketjen black and polyvinylidene (PVDF) with the weight ratio of 70:20:10 were stirred by N-methyl pyrrolidone (NMP) to acquire a uniform slurry. The slurry was then cast on Al foil and dried for 12 h in vacuum and under 100 °C. The areal mass loading of active materials is 1.7 mg/cm^2. To reinforce the Li^+ transportation between cathodes and LLZTO pellets, slight amount (10 μl) of liquid electrolytes (1M $LiPF_6$ and VC in EC: EMC: DMC=1:1:1) was added as the cathode electrolyte, which is commonly used in oxide solid electrolytes. The full cells were measured within the voltage range of 3.0–3.8 V at 30 ℃.

Supporting Information

Supporting Information is available from the Wiley Online Library or from the author.

Conflict of interest

The authors declare that they have no conflict of interest.

Acknowledgements

This work was financially supported by the National Key Research and Development Program of China (No. 2021YFF0500600) and National Natural Science Foundation of China (22209080). H.J. and J.L contributed equally to this work.

Received: ((will be filled in by the editorial staff))
Revised: ((will be filled in by the editorial staff))
Published online: ((will be filled in by the editorial staff))

References

[1] J. B. Goodenough, K. S. Park, *J. Am. Chem. Soc.* **2013**, 135, 1167.

[2] a) P. Albertus, S. Babinec, S. Litzelman, A. Newman, *Nat. Energy* **2017**, 3, 16; b) R. Chen,

This article is protected by copyright. All rights reserved.

Author Manuscript

W. Qu, X. Guo, L. Li, F. Wu, *Mater. Horiz.* **2016**, 3, 487.

[3] a) C. Wang, K. Fu, S. P. Kammampata, D. W. McOwen, A. J. Samson, L. Zhang, G. T. Hitz, A. M. Nolan, E. D. Wachsman, Y. Mo, V. Thangadurai, L. Hu, *Chem. Rev.* **2020**, 120, 4257; b) C. Ma, Y. Cheng, K. Yin, J. Luo, A. Sharafi, J. Sakamoto, J. Li, K. L. More, N. J. Dudney, M. Chi, *Nano Lett.* **2016**, 16, 7030.

[4] a) A. Sharafi, C. G. Haslam, R. D. Kerns, J. Wolfenstine, J. Sakamoto, *J. Mater. Chem. A* **2017**, 5, 21491; b) H. Huo, Y. Chen, J. Luo, X. Yang, X. Guo, X. Sun, *Adv Energy Mater* **2019**, 9, 1804004.

[5] F. Flatscher, M. Philipp, S. Ganschow, H. M. R. Wilkening, D. Rettenwander, *J. Mater. Chem. A* **2020**, 8, 15782.

[6] T. Krauskopf, R. Dippel, H. Hartmann, K. Peppler, B. Mogwitz, F. H. Richter, W. G. Zeier, J. Janek, *Joule* **2019**, 3, 2030.

[7] T. Krauskopf, H. Hartmann, W. G. Zeier, J. Janek, *ACS Appl. Mater. Interfaces* **2019**, 11, 14463.

[8] a) R. Choudhury, M. Wang, J. Sakamoto, *J. Electrochem. Soc.* **2020**, 167, 140501; b) J. Gao, J. Zhu, X. Li, J. Li, X. Guo, H. Li, W. Zhou, *Adv. Funct. Mater.* **2020**, 31, 2001918.

[9] a) T. Krauskopf, F. H. Richter, W. G. Zeier, J. Janek, *Chem. Rev.* **2020**, 120, 7745; b) M. Wang, J. B. Wolfenstine, J. Sakamoto, *Electrochim. Acta* **2019**, 296, 842; c) J. Kasemchainan, S. Zekoll, D. Spencer Jolly, Z. Ning, G. O. Hartley, J. Marrow, P. G. Bruce,

Author Manuscript

This article is protected by copyright. All rights reserved.

Nat. Mater. **2019**, 18, 1105.

[10] a) L. Porz, T. Swamy, B. W. Sheldon, D. Rettenwander, T. Frömling, H. L. Thaman, S. Berendts, R. Uecker, W. C. Carter, Y. M. Chiang, *Adv. Energy Mater.* **2017**, 7, 1701003; b) H. Gao, X. Ai, H. Wang, W. Li, P. Wei, Y. Cheng, S. Gui, H. Yang, Y. Yang, M. S. Wang, *Nat. Commun.* **2022**, 13, 5050.

[11] a) E. J. Cheng, A. Sharafi, J. Sakamoto, *Electrochim. Acta* **2017**, 223, 85; b) Y. Dong, I. W. Chen, J. Li, *Chem. Mater.* **2022**, 34, 5749.

[12] a) W. Luo, Y. Gong, Y. Zhu, Y. Li, Y. Yao, Y. Zhang, K. K. Fu, G. Pastel, C. F. Lin, Y. Mo, E. D. Wachsman, L. Hu, *Adv. Mater.* **2017**, 29, 1606042; b) C. Wang, Y. Gong, B. Liu, K. Fu, Y. Yao, E. Hitz, Y. Li, J. Dai, S. Xu, W. Luo, E. D. Wachsman, L. Hu, *Nano Lett.* **2017**, 17, 565; c) K. Fu, Y. Gong, B. Liu, Y. Zhu, S. Xu, Y. Yao, W. Luo, C. Wang, S. D. Lacey, J. Dai, Y. Chen, Y. Mo, E. Wachsman, L. Hu, *Sci. Adv.* **2017**, 3, e1601659.

[13] M. Yang, Y. Liu, A. M. Nolan, Y. Mo, *Adv. Mater.* **2021**, 33, 2008081.

[14] a) Y. Lu, C.-Z. Zhao, J.-K. Hu, S. Sun, H. Yuan, Z.-H. Fu, X. Chen, J.-Q. Huang, M. Ouyang, Q. Zhang, *Sci. Adv.* **2022**, 8, eadd0510; b) A. Schröder, J. Fleig, D. Gryaznov, J. Maier, W. Sitte, *J. Phys. Chem. B* **2006**, 110 25, 12274.

[15] a) A. Sharafi, H. M. Meyer, J. Nanda, J. Wolfenstine, J. Sakamoto, *J. Power Sources* **2016**, 302, 135; b) M. J. Wang, E. Carmona, A. Gupta, P. Albertus, J. Sakamoto, *Nat. Commun.* **2020**, 11, 5201; c) J. M. Doux, H. Nguyen, D. H. S. Tan, A. Banerjee, X. Wang, E. A. Wu, C. Jo, H. Yang, Y. S. Meng, *Adv. Energy Mater.* **2019**, 10, 1903253.

Author Manuscript

This article is protected by copyright. All rights reserved.

[16] a) L. Chen, R.-A. Tong, J. Zhang, H. Wang, G. Shao, Y. Dong, C.-A. Wang, *Angew. Chem. Int. Ed.* **2023**, 62, e202305099; b) M. Gao, Z. Gong, H. Li, H. Zhao, D. Chen, Y. Wei, D. Li, Y. Li, L. Yang, Y. Chen, *Adv. Funct. Mater.* **2023**, 33, 2300319.

[17] a) K. Lee, S. Han, J. Lee, S. Lee, J. Kim, Y. Ko, S. Kim, K. Yoon, J.-H. Song, J. H. Noh, K. Kang, *ACS Energy Lett.* **2021**, 7, 381; b) Z. Bi, Q. Sun, M. Jia, M. Zuo, N. Zhao, X. Guo, *Adv Funct Mater* **2022**, 32, 2208751.

[18] S. Kim, J. S. Kim, L. Miara, Y. Wang, S. K. Jung, S. Y. Park, Z. Song, H. Kim, M. Badding, J. Chang, V. Roev, G. Yoon, R. Kim, J. H. Kim, K. Yoon, D. Im, K. Kang, *Nat. Commun.* **2022**, 13, 1883.

[19] Y. Ren, H. Deng, R. Chen, Y. Shen, Y. Lin, C.-W. Nan, *J. Eur. Ceram. Soc.* **2015**, 35, 561.

[20] H. Zheng, S. Wu, R. Tian, Z. Xu, H. Zhu, H. Duan, H. Liu, *Adv. Funct. Mater.* **2019**, 30, 1906189.

[21] a) S. Chen, Z. Nie, F. Tian, L. Nie, R. Wei, J. Yu, T. Gao, Z. Sun, N. Yang, W. Liu, *Adv. Funct. Mater.* **2022**, 32, 2113318; b) A. Sharafi, E. Kazyak, A. L. Davis, S. Yu, T. Thompson, D. J. Siegel, N. P. Dasgupta, J. Sakamoto, *Chem. Mater.* **2017**, 29, 7961.

[22] Y. Huang, B. Chen, J. Duan, F. Yang, T. Wang, Z. Wang, W. Yang, C. Hu, W. Luo, Y. Huang, *Angew. Chem. Int. Ed.* **2020**, 59, 3699.

[23] a) J. Meng, Y. Zhang, X. Zhou, M. Lei, C. Li, *Nat. Commun.* **2020**, 11, 3716; b) N. Syed, A. Zavabeti, J. Z. Ou, M. Mohiuddin, N. Pillai, B. J. Carey, B. Y. Zhang, R. S. Datta, A.

Author Manuscript

This article is protected by copyright. All rights reserved.

Jannat, F. Haque, K. A. Messalea, C. Xu, S. P. Russo, C. F. McConville, T. Daeneke, K. Kalantar-Zadeh, *Nat. Commun.* **2018**, 9, 3618.

[24] M. Muller, J. Schmieg, S. Dierickx, J. Joos, A. Weber, D. Gerthsen, E. Ivers-Tiffee, *ACS Appl. Mater. Interfaces* **2022**, 14, 14739.

[25] T. Wang, J. Duan, B. Zhang, W. Luo, X. Ji, H. Xu, Y. Huang, L. Huang, Z. Song, J. Wen, C. Wang, Y. Huang, J. B. Goodenough, *Energy Environ. Sci.* **2022**, 15, 1325.

[26] X. Miao, H. Wang, R. Sun, X. Ge, D. Zhao, P. Wang, R. Wang, L. Yin, *Adv. Energy Mater.* **2021**, 11, 2003469.

[27] a) B. Hu, W. Yu, B. Xu, X. Zhang, T. Liu, Y. Shen, Y. H. Lin, C. W. Nan, L. Li, *ACS Appl. Mater. Interfaces* **2019**, 11, 34939; b) W. Hu, Y. Yao, X. Huang, S. Ju, Z. Chen, M. Li, Y. Wu, *ACS Appl. Energy Mater.* **2022**, 5, 3773.

[28] a) W. Feng, J. Hu, G. Qian, Z. Xu, G. Zan, Y. Liu, F. Wang, C. Wang, Y. Xia, *Sci. Adv.* **2022**, 8, eadd8972; b) F. Han, A. S. Westover, J. Yue, X. Fan, F. Wang, M. Chi, D. N. Leonard, N. J. Dudney, H. Wang, C. Wang, *Nat. Energy* **2019**, 4, 187; c) X. Liu, R. Garcia-Mendez, A. R. Lupini, Y. Cheng, Z. D. Hood, F. Han, A. Sharafi, J. C. Idrobo, N. J. Dudney, C. Wang, C. Ma, J. Sakamoto, M. Chi, *Nat. Mater.* **2021**, 20, 1485.

[29] S. Tang, G. Chen, F. Ren, H. Wang, W. Yang, C. Zheng, Z. Gong, Y. Yang, *J. Mater. Chem. A* **2021**, 9, 3576.

[30] a) Y. C. Chen, C. Y. Ouyang, L. J. Song, Z. L. Sun, *J. Phys. Chem. C* **2011**, 115, 7044; b)

Author Manuscript

This article is protected by copyright. All rights reserved.

J. Shi, P. Li, K. Han, D. Sun, W. Zhao, Z. Liu, G. Liang, K. Davey, Z. Guo, X. Qu, *Energy Storage Mater.* **2022**, 51, 306.

[31] W. P. Chen, H. Duan, J. L. Shi, Y. Qian, J. Wan, X. D. Zhang, H. Sheng, B. Guan, R. Wen, Y. X. Yin, S. Xin, Y. G. Guo, L. J. Wan, *J. Am. Chem. Soc.* **2021**, 143, 5717.

[32] S. Lee, K.-s. Lee, S. Kim, K. Yoon, S. Han, M. H. Lee, Y. Ko, J. H. Noh, W. Kim, K. Kang, *Sci. Adv.* **2022**, 8, eabq0153.

[33] H. Huo, Y. Chen, N. Zhao, X. Lin, J. Luo, X. Yang, Y. Liu, X. Guo, X. Sun, *Nano Energy* **2019**, 61, 119.

[34] H. Wang, H. Gao, X. Chen, J. Zhu, W. Li, Z. Gong, Y. Li, M. S. Wang, Y. Yang, *Adv. Energy Mater.* **2021**, 11, 2102148.

[35] Q. Ma, T. Ortmann, A. Yang, D. Sebold, S. Burkhardt, M. Rohnke, F. Tietz, D. Fattakhova-Rohlfing, J. Janek, O. Guillon, *Adv. Energy Mater.* **2022**, 12, 2201680.

[36] H. Koshikawa, S. Matsuda, K. Kamiya, M. Miyayama, Y. Kubo, K. Uosaki, K. Hashimoto, S. Nakanishi, *J. Power Sources* **2018**, 376, 147.

[37] D. Lu, Y. Shao, T. Lozano, W. D. Bennett, G. L. Graff, B. Polzin, J. Zhang, M. H. Engelhard, N. T. Saenz, W. A. Henderson, P. Bhattacharya, J. Liu, J. Xiao, *Adv. Energy Mater.* **2015**, 5, 1400993.

[38] a) D. Aurbach, E. Zinigrad, H. Teller, P. Dan, *J. Electrochem. Soc.* **2000**, 147, 1274; b) D. Aurbach, E. Zinigrad, Y. Cohen, H. Teller, *Solid State Ionics* **2002**, 148, 405.

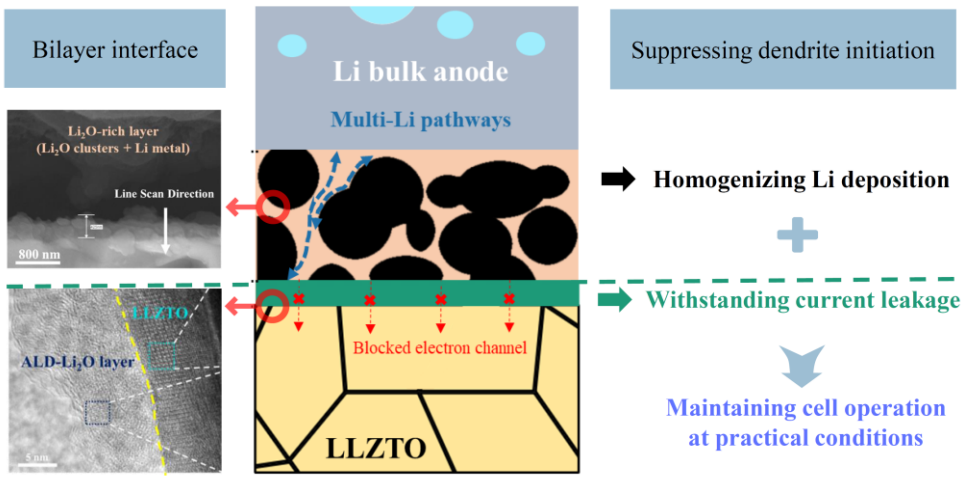
Author Manuscript

This article is protected by copyright. All rights reserved.

Solid-state batteries with metallic Li anodes are of great interest for next-generation power sources; however, their practical application is restricted by detrimental Li dendrites. Here, we analyze the dendrite inducement factors when cycling at moderate temperature without external stack pressure, and introduce a bilayer Li_2O-rich interfacial structure that can effectively prolong cycling stability even at high current densities.

Haoyang Jiang, Junqing Liu, Bin Tang,* Zhendong Yang, Xinghui Liang, Xinyu Yu, Yirong Gao, Jinping Wei, and Zhen Zhou*

Regulation Mechanism on a Bilayer Li_2O-Rich Interface between Lithium Metal and Garnet-Type Solid Electrolytes



Author Manuscript

This article is protected by copyright. All rights reserved.